

Scientific Machine Learning Based Reduced-Order Models for Plasma Turbulence Simulations

Constantin Gahr,^{1, a)} Ionuț-Gabriel Farcaș,^{2, 3, b)} and Frank Jenko^{1, c)}

¹⁾Max Planck Institute for Plasma Physics, 85748 Garching, Germany^{d)}

²⁾Oden Institute for Computational Engineering and Sciences, The University of Texas at Austin, Austin, TX 78712

³⁾Department of Mathematics, Virginia Tech, Blacksburg, VA 24061^{d)}

(Dated: June 27, 2024)

This paper focuses on the construction of non-intrusive Scientific Machine Learning (SciML) Reduced-Order Models (ROMs) for plasma turbulence simulations. In particular, we propose using Operator Inference (OpInf) to build low-cost physics-based ROMs from data for such simulations. As a representative example, we focus on the Hasegawa-Wakatani (HW) equations used for modeling two-dimensional electrostatic drift-wave turbulence. For a comprehensive perspective of the potential of OpInf to construct accurate ROMs, we consider three setups for the HW equations by varying a key model parameter, namely the adiabaticity coefficient. These setups lead to the formation of complex and nonlinear dynamics, which makes the construction of accurate ROMs of any kind challenging. We generate the training datasets by performing direct numerical simulations of the HW equations and recording the computed state data and outputs over a time horizon of 100 time units in the turbulent phase. We then use these datasets to construct OpInf ROMs for predictions over 400 additional time units. Our results show that the OpInf ROMs capture the important features of the turbulent dynamics and generalize beyond the training time horizon while reducing the computational effort of the high-fidelity simulation by up to five orders of magnitude. In the broader context of fusion research, this shows that non-intrusive SciML ROMs have the potential to drastically accelerate numerical studies, which can ultimately enable tasks such as the design of optimized fusion devices.

I. INTRODUCTION

Understanding, predicting, and controlling turbulent transport in magnetic confinement devices is critical towards commercially viable fusion. High-fidelity simulations of turbulent transport, despite tremendous progress, remain impractical for many design or control tasks due to their high computational cost even on powerful supercomputers. This necessitates the development of innovative reduced modeling approaches to enable these tasks at scale.

Simulations of plasma turbulence in fusion devices have been revolutionised through high-performance computing, facilitating the transition from merely qualitative to quantitative and detailed predictions. Furthermore, the recent emergence of exascale-capable machines¹ paves the way towards full-device² and complex multi-scale turbulent transport simulations². However, these simulations often require significant resources even on large supercomputers, thus restricting the number of cases that can be studied explicitly. This, in turn, prohibits the routine use of high-fidelity models for many-query tasks that require ensembles of simulations such as the design and control of optimized fusion devices, or uncertainty quantification and sensitivity analysis³. An alternative is provided by Reduced-Order Models (ROMs)^{4,5} which aim to construct computationally cheap but sufficiently accurate approximations of high-fidelity models with the goal of replacing them for the aforementioned tasks.

In recent years, Scientific Machine Learning (SciML) developed tools for building ROMs for complex applications by combining the rigor of physics-based modeling with the convenience of data-driven learning. In essence, given data stemming from numerical simulations or experimental measurements (or both), SciML constructs ROMs by embedding physics principles into the learning problem.

In the present paper, we focus on constructing SciML ROMs for complex, nonlinear plasma turbulence models. Our goal is to demonstrate that such ROMs can provide predictions with sufficient accuracy while reducing the computational cost of the high-fidelity simulation code by orders of magnitude. In particular, we focus on Operator Inference (OpInf)^{6,7}. OpInf is a SciML approach for learning physics-based reduced models from data for models with polynomial structure. More general types of nonlinearities can be considered as well by making use of lifting transformations^{8,9} that expose polynomial structure in the lifted governing equations. OpInf was used to construct ROMs for complex applications such as reactive flows in rocket engines^{10–12}, solar wind predictions in space weather applications¹³, solidification simulations¹⁴, and chaotic systems¹⁵ such as Lorenz 96 and the Kuramoto-Sivashinsky equations. Extensions include using filtering¹⁶ and roll-outs¹⁷ to handle noisy, scarce, and low-quality data, and localization¹⁸, domain decomposition¹⁹, and quadratic manifolds²⁰ to address some of the challenges in reducing problems with complex dynamics. The recent review paper⁷ provides a comprehensive overview on OpInf.

The plasma turbulence model under consideration is given by the Hasegawa-Wakatani (HW) equations²¹. They model two-dimensional electrostatic drift-wave turbulence in a slab geometry and have been studied extensively^{22–24}. The dynamics of these equations were analyzed using Proper Orthogo-

^{a)}Electronic mail: constantin.gahr@ipp.mpg.de

^{b)}Electronic mail: ionut.farcas@austin.utexas.edu

^{c)}Electronic mail: frank.jenko@ipp.mpg.de

^{d)}C. Gahr and I. Farcaș contributed equally to this work

nal Decomposition (POD)^{25,26}, a classical ROM approach²⁷. Furthermore, Ref.²⁸ constructed ROMs for the linearized HW equations using balanced truncation. In recent years, significant progress has been made in developing neural network approximations for the HW equations, including initial turbulent state predictions²⁹, closure models for Large Eddy Simulations³⁰, surrogate models for transport simulations³¹, direct particle flux predictions³², and synthesized impurity structures³³. Further studies related to plasma physics beyond the HW equations include Ref.^{34–37} which used Dynamic Mode Decomposition (DMD) and POD for analyzing plasma dynamics, Refs.^{38,39} which used these methods for constructing ROMs for predictions beyond their training time horizon, Ref.⁴⁰ which used neural networks to approximate quantities of interest (QoIs) such as the particle flux, and Ref.⁴¹ which used neural operators to construct surrogates. However, constructing accurate and predictive ROMs for complex plasma turbulence simulations remains a challenging task.

In this work, we take a step forward in this direction and propose using OpInf for constructing computationally cheap SciML ROMs for key QoIs in the HW equations, namely the particle flux and resistive dissipation rate. These two QoIs represent the dominant energy source and sink in the HW model and are therefore ubiquitous for assessing turbulent transport. Since their time evolution is complex and exhibits chaotic behaviour, constructing ROMs of any kind is non-trivial. Our goal in the present paper is to show that OpInf can be used to construct ROMs that provide statistically accurate predictions for the key QoI while reducing the cost of the high-fidelity simulation by orders of magnitude. To gain a broader understanding, we explore three distinct setups where a key parameter in the governing equations, the adiabaticity coefficient, is varied. For each setup, the OpInf ROM is employed to generate predictions over a time horizon four times longer than the training horizon. We note that to the best of our knowledge, this represents one of the first studies in which SciML ROMs are considered for the HW equations.

The remainder of the paper is organized as follows. Section II summarizes the HW equations, the relevant QoI, and the setup for high-fidelity numerical simulations. Section III presents the steps to construct physics-based data-driven ROMs via OpInf for the HW system. Section IV presents our numerical results and discusses our findings. We conclude the paper in Section V.

II. MODELING PLASMA TURBULENCE VIA THE HASEGAWA-WAKATANI EQUATIONS

This section summarizes the HW equations for modeling two-dimensional electrostatic drift-wave turbulence. Section II A provides the physics background. Section II B presents the HW equations, followed by Section II C, which presents the two most relevant QoIs. Section II D provides the setup for solving the HW equations numerically.

A. Physics background

The HW equations represent a nonlinear two-dimensional fluid model for drift-wave turbulence in magnetized plasmas^{21,22,42}. They model the fluctuations of the plasma density and potential in a plane perpendicular to the magnetic field and in the presence of a background density gradient.

In this model, the magnetic field is assumed to be homogeneous and constant in the z -direction. The background density $n_0(x, y) = n_0(x)$ is non-uniform in the x -direction and has a constant equilibrium density scale $L_n = |\partial_x \log n_0|^{-1}$. The gradient in the background density transports particles in the positive x -direction, which continuously introduces energy and drives the turbulent transport in the system.

The spatial and temporal coordinates as well as the fields are rescaled to be dimensionless. Following²², let \bar{x} , \bar{y} , and \bar{t} represent the two spatial and time coordinates in Gaussian Centimeter-Gram-Second (CGS) units. The inverse of the sound radius $\rho_s = c_s/\omega_{ci}$ scales the spatial coordinates to $x = \bar{x}/\rho_s$ and $y = \bar{y}/\rho_s$, respectively, where $c_s = \sqrt{T_e/m_i}$ denotes the ion sound speed and $\omega_{ci} = eB_0/(m_i c)$ is the ion cyclotron frequency, where T_e is the electron temperature, m_i represents the ion mass, e is the electric charge, B_0 is the magnetic field strength, and c is the speed of light. The electron drift frequency $\omega_{de} = c_s/L_n$ scales the time component to $t = \bar{t}\omega_{de}$. The normalized density and potential fluctuations \tilde{n} and $\tilde{\phi}$ are obtained from the original fields \bar{n} and $\bar{\phi}$ as

$$\tilde{n} = \frac{\bar{n} L_n}{n_0 \rho_s} \quad \text{and} \quad \tilde{\phi} = \frac{e\bar{\phi} L_n}{T_e \rho_s}. \quad (1)$$

B. The Hasegawa-Wakatani equations

The HW equations describe the time evolution of density \tilde{n} and potential $\tilde{\phi}$ fluctuations in a two-dimensional slab geometry of size $L \times L$ under the influence of the background magnetic field and the background density gradient. They read

$$\begin{cases} \partial_t \nabla^2 \tilde{\phi} &= c_1 (\tilde{\phi} - \tilde{n}) - \{\tilde{\phi}, \nabla^2 \tilde{\phi}\} + \nu \nabla^{2N} \nabla^2 \tilde{\phi} \\ \partial_t \tilde{n} &= c_1 (\tilde{\phi} - \tilde{n}) - \{\tilde{\phi}, \tilde{n}\} - \partial_y \tilde{\phi} + \nu \nabla^{2N} \tilde{n}, \end{cases} \quad (2)$$

where $\nabla^2 \tilde{\phi}$ is the vorticity and $\{f, g\} := \partial_x f \partial_y g - \partial_y f \partial_x g$ denotes the Poisson bracket of f and g . The adiabaticity parameter $c_1 > 0$ controls how fast the electric potential reacts to changes in the density and exerts a significant impact on the dynamics of these equations. In the limit $c_1 \rightarrow \infty$, the potential reacts instantaneously to changes in the density and the model reduces to the Hasegawa-Mima equation⁴³. In the other extreme, $c_1 \rightarrow 0$ decouples the density and potential fluctuations and the model reduces to the Navier-Stokes equations²². The hyperdiffusion terms ∇^{2N} are introduced to prevent energy accumulation at the grid scale, with the hyperdiffusivity coefficient ν controlling the amount of dissipated energy. Periodic boundary conditions are assumed in both spatial directions. After initialization, the dynamics undergo a transient phase in which drift-waves dominate the dynamics and the energy grows exponentially. The dynamics subsequently enter the

turbulent phase, where the effect of nonlinearities becomes significant and turbulent transport dominates.

C. Energy balance and quantities of interest

The gradient in the background density continuously transports particles from the background density n_0 to the fluctuating density \tilde{n} , therefore driving the turbulent dynamics. The particle flux Γ_n measures the rate at which particles enter the system and is defined as

$$\Gamma_n(t) = -\frac{1}{L^2} \int d\mathbf{x} \tilde{n}(t, \mathbf{x}) \partial_y \tilde{\phi}(t, \mathbf{x}), \quad (3)$$

where $d\mathbf{x} = dx dy$ and $\mathbf{x} = (x, y)$. At the same time, energy is resistively dissipated. Resistive dissipation constitutes the main energy sink and is quantified by Γ_c defined as

$$\Gamma_c(t) = \frac{c_1}{L^2} \int d\mathbf{x} (\tilde{n}(t, \mathbf{x}) - \tilde{\phi}(t, \mathbf{x}))^2. \quad (4)$$

These two quantities represent the dominant energy source and sink in the HW model. In the turbulent phase, nonlinear saturation occurs when the particle flux and the resistive dissipation rate balance. Given their importance for assessing turbulent transport in the HW equations, Γ_n and Γ_c represent the QoIs in our numerical experiments. Our main goal in the present paper is to construct low-cost data-driven ROMs that can accurately and reliably predict these two quantities.

D. Setup for Direct Numerical Simulations

We solve the HW equations (2) numerically using Direct Numerical Simulations (DNS)⁴⁴. The computational domain has a 2D slab geometry of size $L \times L = (2\pi/k_0)^2$ with $k_0 = 0.15$. It is discretized using an equidistant grid comprising $N_x = 512 \times 512 = 262,144$ spatial degrees of freedom. Since we have $N_s = 2$ state variables, the total number of degrees of freedom is $N_{\text{state}} = N_s \times N_x = 524,288$.

The Poisson brackets are discretized using a 4th-order Arakawa scheme⁴⁵. The remaining spatial derivatives, including the one in (3), are discretized using 2nd-order finite differences. The time iterations consist of two steps. First, the HW equations (2) are solved using the explicit 4th-order Runge-Kutta method⁴⁶ resulting in the density \tilde{n} and vorticity $\nabla^2 \tilde{\phi}$. In the second step, the Poisson equation $\nabla^2 \tilde{\phi}$ is solved using spectral methods to compute $\tilde{\phi}$. The $N_{\text{out}} = 2$ QoIs (3) and (4) are then estimated using the trapezoidal rule.

The equations are solved in increments of $\delta_t = 0.01$. The initial conditions are instances of a 2D Gaussian random field with zero mean and covariance $0.01 \times \text{Id}$. The diffusivity parameter is $\nu = 5 \cdot 10^{-9}$ with hyperdiffusion order $N = 3$. A reference implementation is available at <https://github.com/the-rccg/hw2d>⁴⁴.

To obtain a comprehensive perspective, we consider three values for the adiabaticity parameter c_1 , namely $c_1 = 0.1$ (close to the hydrodynamic limit), the typically studied intermediate value $c_1 = 1.0$, and $c_1 = 5.0$ (with adiabatic electrons

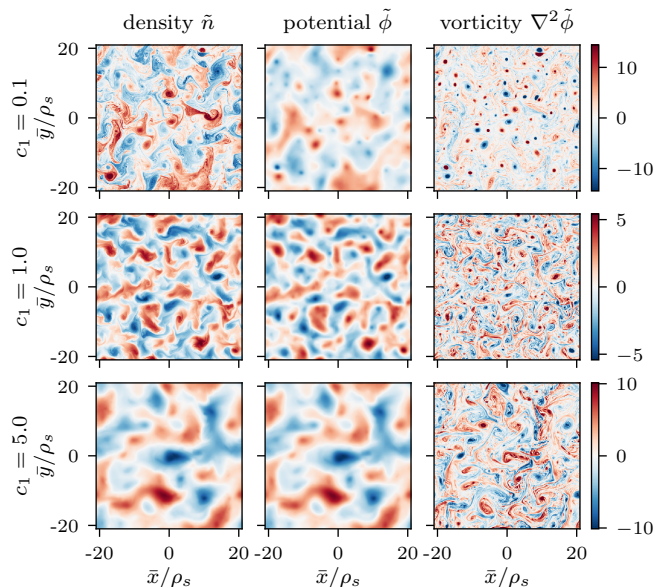


Figure 1. Density fluctuations \tilde{n} , potential fluctuations $\tilde{\phi}$, and normalized vorticity $\nabla^2 \tilde{\phi}$ for $c_1 \in \{0.1, 1.0, 5.0\}$.

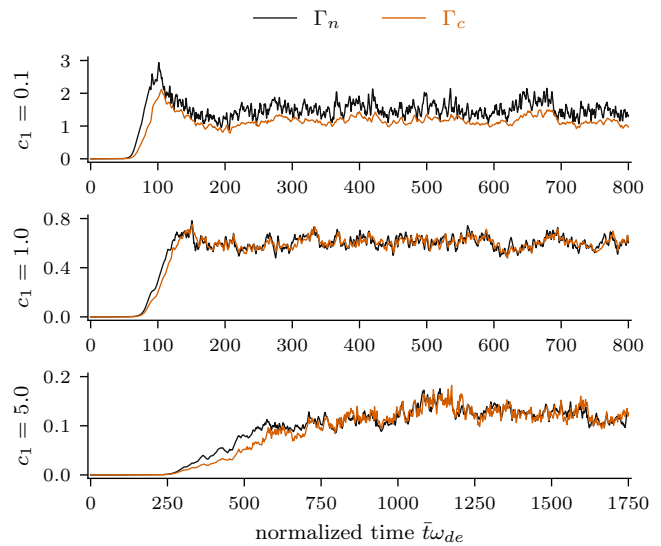


Figure 2. Example particle flux Γ_n and resistive dissipation rate Γ_c from initialization to nonlinear saturation.

towards the Hasegawa-Mima limit). Figure 1 plots examples of density, potential, and (normalized) vorticity fields in the turbulent regime for these three values. Note that the similarity between density and potential increases with c_1 . All c_1 values lead to the formation of complex, nonlinear and self-driven dynamics, rendering the construction of accurate and predictive ROMs of any kind challenging.

The three DNS were performed over a sufficiently long time horizon to capture enough time steps within the turbulent regime. This ensures a thorough assessment of the predictive capabilities of our OpInf ROMs. Figure 2 plots the

two QoIs starting from $t = 0$ for the three values of c_1 . The onset of turbulent-driven transport increases with c_1 . Because of this, the DNS for $c_1 = 0.1$ and $c_1 = 1.0$ were performed over time horizon $[0, 800]$, each requiring about 16 hours on a single core of an Intel(R) Xeon(R) 6148 CPU. The DNS for $c_1 = 5.0$ was performed over $[0; 1, 750]$, necessitating roughly 35 hours on a single core. In our OpInf experiments, we will focus on time horizons that ensure that the turbulent dynamics are fully developed, namely $t \geq 300$ for $c_1 = 0.1$ and $c_1 = 1.0$, and $t \geq 1, 250$ for $c_1 = 5.0$.

III. LEARNING PHYSICS-BASED REDUCED MODELS FROM DATA FOR THE HASEGAWA-WAKATANI SYSTEM VIA OPERATOR INFERENCE

We propose using OpInf to construct computationally inexpensive data-driven ROMs for the HW system. Section III A summarizes the OpInf setup followed by Section III B which presents the steps to construct OpInf ROMs.

A. Preliminaries

We start by identifying the structure of the governing equations. In the context of OpInf, the governing equations are generally written in semi-discrete form after discretizing the underlying partial differential equation (PDE) model in space. For the HW equations, the spatial discretization of the state equations (2) and the estimation of the QoIs (3) and (4) using the steps summarized in Section II D allows writing the governing and output equations in semi-discrete form as a quadratic system of coupled equations,

$$\dot{\mathbf{q}}(t) = \mathbf{A}\mathbf{q}(t) + \mathbf{H}(\mathbf{q}(t) \otimes \mathbf{q}(t)) \quad (5a)$$

$$\mathbf{y}(t) = \mathbf{G}(\mathbf{q}(t) \otimes \mathbf{q}(t)), \quad (5b)$$

where $\mathbf{q}(t) = (\tilde{\mathbf{n}}(t) \ \tilde{\boldsymbol{\phi}}(t))^\top \in \mathbb{R}^{N_{\text{state}}}$ denotes the spatially discretized state variables at time t and $\mathbf{y}(t) = (\Gamma_n(t) \ \Gamma_c(t))^\top \in \mathbb{R}^{N_{\text{out}}}$ the corresponding outputs, $\mathbf{A} \in \mathbb{R}^{N_{\text{state}} \times N_{\text{state}}}$ and $\mathbf{H} \in \mathbb{R}^{N_{\text{state}} \times N_{\text{state}}^2}$ denote the linear and quadratic state operators, and $\mathbf{G} \in \mathbb{R}^{N_{\text{out}} \times N_{\text{state}}^2}$ denotes the quadratic output operator, where $N_{\text{state}} = 524, 288$ and $N_{\text{out}} = 2$. We consider the time evolution of (5) over a time horizon $[t_{\text{init}}, t_{\text{final}}]$ in the turbulent phase, with t_{init} denoting the initial and t_{final} the final time. The initial condition in (5a) is the high-dimensional state solution at $t = t_{\text{init}}$. We refer to (5) as the *HW system*.

We consider the setup where we are given a training dataset over a time horizon $[t_{\text{init}}, t_{\text{train}}]$ with $t_{\text{train}} < t_{\text{final}}$ obtained by solving the HW system using the setup from Section II D and recording the corresponding state vectors $\mathbf{q}_i = \mathbf{q}(t_i)$ and outputs $\mathbf{y}_i = \mathbf{y}(t_i)$ at n_t time instants $t_i \in [t_{\text{init}}, t_{\text{train}}]$. The two sets of solutions are assembled into a snapshot matrix $\mathbf{Q} \in \mathbb{R}^{N_{\text{state}} \times n_t}$ and an output matrix $\mathbf{Y} \in \mathbb{R}^{N_{\text{out}} \times n_t}$ as

$$\mathbf{Q} = \begin{bmatrix} | & | & & | \\ \mathbf{q}_1 & \mathbf{q}_2 & \dots & \mathbf{q}_{n_t} \\ | & | & & | \end{bmatrix} \quad \text{and} \quad \mathbf{Y} = \begin{bmatrix} | & | & & | \\ \mathbf{y}_1 & \mathbf{y}_2 & \dots & \mathbf{y}_{n_t} \\ | & | & & | \end{bmatrix},$$

with the state vectors \mathbf{q}_i and outputs \mathbf{y}_i as their respective i th columns. Given \mathbf{Q} and \mathbf{Y} , our goal is to construct OpInf ROMs that capture the features and the statistical properties of the outputs beyond the training time horizon.

B. Learning physics-based data-driven reduced models via Operator Inference

OpInf is a SciML approach that combines the perspectives of physics-based modeling with data-driven learning to non-intrusively construct computationally cheap ROMs of systems with polynomial nonlinearities from data⁶. For more general types of nonlinearities, lifting transformations⁹ can be used to expose polynomial structure in the lifted governing equations. OpInf requires two main ingredients: knowledge about the structure of the governing equations and a training data set to construct a structure-preserving ROM. The HW system (5) is quadratic in both state and output. The steps to construct quadratic ROMs via OpInf are outlined below.

The snapshot matrix \mathbf{Q} is used to compute a rank- r linear POD basis to represent the high-dimensional state snapshots in a low-dimensional subspace spanned by the basis vectors. One of the most prevalent methods for determining this basis is based on the thin singular value decomposition of the snapshot matrix⁴⁷

$$\mathbf{Q} = \mathbf{V}\boldsymbol{\Sigma}\mathbf{W}^\top,$$

where $\mathbf{V} \in \mathbb{R}^{N_{\text{state}} \times n_t}$ contains the left singular vectors, $\mathbf{W} \in \mathbb{R}^{n_t \times n_t}$ contains the right singular vectors. $\boldsymbol{\Sigma} \in \mathbb{R}^{n_t \times n_t}$ is a diagonal matrix with the singular values arranged on the diagonal in non-increasing order $\sigma_i \geq \sigma_{i+1}$ for $i = 1, 2, \dots, n_t - 1$. The rank- r POD basis $\mathbf{V}_r \in \mathbb{R}^{N_{\text{state}} \times r}$ consists of the first $r \ll N_{\text{state}}$ columns of \mathbf{V} , i.e., the left singular vectors corresponding to the r largest singular values. We note that in problems with multiple state variables with different scales, it is recommended to center and scale the training snapshots variable-by-variable prior to computing the POD basis. For example, in settings targeting ROMs for dynamics close to or within their steady-state/saturated region, each variable can be centered with respect to its mean over the training horizon and then scaled with respect to its maximum absolute value.

The representation of the high-dimensional state snapshots in the low-dimensional subspace spanned by the POD basis vectors is computed as

$$\hat{\mathbf{q}}_i = \mathbf{V}_r^\top \mathbf{q}_i \in \mathbb{R}^r \quad \text{for } i = 1, 2, \dots, n_t. \quad (6)$$

The reduced states $\hat{\mathbf{q}}_i$ are then recorded as columns into a matrix $\hat{\mathbf{Q}} \in \mathbb{R}^{r \times n_t}$. The dimension of the output \mathbf{Y} remains unchanged. Analogously to the state data, multi-dimensional outputs with different scales may need to be centered and scaled prior to constructing ROMs.

OpInf then learns the reduced operators for a structure-preserving quadratic ROM from data given by $\hat{\mathbf{Q}}$ and \mathbf{Y} :

$$\dot{\hat{\mathbf{q}}}(t) = \hat{\mathbf{A}}\hat{\mathbf{q}}(t) + \hat{\mathbf{H}}(\hat{\mathbf{q}}(t) \otimes \hat{\mathbf{q}}(t)) \quad (7a)$$

$$\hat{\mathbf{y}}(t) = \hat{\mathbf{G}}(\hat{\mathbf{q}}(t) \otimes \hat{\mathbf{q}}(t)), \quad (7b)$$

where $\hat{\mathbf{A}} \in \mathbb{R}^{r \times r}$, $\hat{\mathbf{H}} \in \mathbb{R}^{r \times r^2}$, and $\hat{\mathbf{G}} \in \mathbb{R}^{N_{\text{out}} \times r^2}$. Moreover, $\hat{\mathbf{y}}(t) \in \mathbb{R}^{N_{\text{out}}}$ denotes the output ROM approximation. The reduced operators are inferred by solving two least-square minimizations, one for the reduced state dynamics

$$\arg \min_{\hat{\mathbf{A}}, \hat{\mathbf{H}}} \sum_{i=1}^{n_t} \left\| \dot{\hat{\mathbf{q}}}_i - \hat{\mathbf{A}} \hat{\mathbf{q}}_i - \hat{\mathbf{H}} (\hat{\mathbf{q}}_i \otimes \hat{\mathbf{q}}_i) \right\|_2^2 + \beta_A \|\hat{\mathbf{A}}\|_F^2 + \beta_H \|\hat{\mathbf{H}}\|_F^2, \quad (8)$$

and the other for the outputs

$$\arg \min_{\hat{\mathbf{G}}} \sum_{i=1}^{n_t} \left\| \hat{\mathbf{y}}_i - \hat{\mathbf{G}} (\hat{\mathbf{q}}_i \otimes \hat{\mathbf{q}}_i) \right\|_2^2 + \beta_G \|\hat{\mathbf{G}}\|_F^2, \quad (9)$$

where $\|\cdot\|_2$ denotes the 2-norm and $\|\cdot\|_F$ is the Frobenius norm. In the learning problem (8), $\dot{\hat{\mathbf{q}}}_i \in \mathbb{R}^r$ denotes the projected time derivative of the i th snapshot vector. If the numerical code provides the high-dimensional time derivative $\dot{\mathbf{q}}_i \in \mathbb{R}^N$, $\dot{\hat{\mathbf{q}}}_i$ is obtained as $\dot{\hat{\mathbf{q}}}_i = \mathbf{V}_r^\top \dot{\mathbf{q}}_i$. Otherwise, it must be estimated numerically via finite differences, for example. However, least-squares minimizations are known to be sensitive to right-hand-side perturbations⁴⁷, hence an inaccurate approximation of $\dot{\hat{\mathbf{q}}}_i$ will have a deleterious influence on the minimization solution, especially in chaotic systems such as the HW equations considered in the present work. In such cases, using the time-discrete formulation of OpInf is preferred¹⁶. Therein, the right-hand side of (8) is obtained by time-shifting the left-hand side to the right by one as done in DMD, which learns discrete linear ROMs.

Following⁴⁸, Tikhonov regularization with separate regularization hyperparameters for linear and quadratic reduced operators is used to reduce overfitting or to compensate for other possible errors and model misspecifications. It plays a key role in constructing predictive OpInf ROMs in problems with complex dynamics, and it will be crucial in the present work as well. Refs.^{11,48} proposed determining the regularization hyperparameters in (8) via a two-dimensional grid search over candidate values for each reduced operator. The optimal regularization pair is the one that minimizes the training error subject to a constraint that the learned reduced coefficients have bounded growth within a trial time horizon $[t_{\text{init}}, t_{\text{trial}}]$ with $t_{\text{trial}} \geq t_{\text{final}}$. This can be extended to also finding the optimal regularization hyperparameter for the reduced output equation (9). However, deterministic procedures that aim to find a single regularization set of parameter may struggle with chaotic systems such as the HW system.

We propose a different, statistical strategy that computes an ensemble of solutions, as follows. We consider a set of candidate regularization pairs $\mathcal{B}_{\text{state}} \subset \mathbb{R}_{>0}^2$ for (8) and a set of candidate regularization parameters $\mathcal{B}_{\text{out}} \subset \mathbb{R}_{>0}$ for (9). For each element of $(\beta_A, \beta_H) \in \mathcal{B}_{\text{state}}$, we solve (8) to find the reduced state operators, which are then used to compute the reduced state solution over the target time horizon $[t_{\text{init}}, t_{\text{final}}]$ by solving (7a). Next, we compute the reduced output operator by solving (9) for each candidate $\beta_G \in \mathcal{B}_{\text{out}}$, and plug the reduced state solution of the previous step into the reduced output equation (7b) to determine the approximate output over $[t_{\text{init}}, t_{\text{final}}]$. We note that these steps are computationally cheap as they depend on the reduced dimension $r \ll N_{\text{state}}$. We then

extract the two QoIs from the approximate output and compute their respective means and standard deviations over both training and prediction time horizons. Exploiting the fact that in the turbulent phase the statistics of the QoIs over the training and prediction horizons are similar, we compute the relative errors of their means and standard deviations with respect to the high-fidelity means and standard deviations over the training horizon. The ensemble of solutions comprises all approximate outputs with relative errors falling below user-prescribed tolerances. We note that typically, an accurately approximated mean suffices since in real-world experiments the QoIs are time-averaged quantities. However, we additionally compare the standard deviations for a more in-depth assessment of the ROM approximations.

IV. NUMERICAL EXPERIMENTS AND DISCUSSION

We now employ OpInf to learn physics-based ROMs for the HW system. Section IV A summarizes the setup for OpInf. We report our results in Section IV B. The impact of changing the initial condition to generate training data on OpInf ROMs is discussed in Section IV C. All ROM calculations were performed on a shared-memory machine with 256 AMD EPYC 7702 CPUs and 2 TB of RAM, using the `numpy`⁴⁹ and `scipy`⁵⁰ scientific computing libraries in python.

A. Setup for Operator Inference

We construct OpInf ROMs for $c_1 \in \{0.1, 1.0, 5.0\}$. The training datasets are obtained by solving the governing equations and computing the corresponding outputs using the setup summarized in Section II D, and recording the computed high-dimensional state vectors and outputs at every second time iteration in the turbulent regime, that is, by downsampling the simulation results by a factor of two. The three initial conditions are distinct realization of the mean-free 2D Gaussian random field with covariance $0.01 \times \text{Id}$. We consider the setup in which training data are provided for 100 time units, for which we have $n_t = 5,000$ state snapshots and outputs. Therefore, $\mathbf{Q} \in \mathbb{R}^{524,288 \times 5,000}$ and $\mathbf{Y} \in \mathbb{R}^{2 \times 5,000}$. The training horizon for $c_1 = 0.1$ and $c_1 = 1.0$ begins at $t_{\text{init}} = 300$, and at $t_{\text{init}} = 1,250$ for $c_1 = 5.0$.

We start by computing the three POD bases using the given DNS snapshot data. Figure 3 plots the POD singular values on the left and the corresponding retained energy on the right. The decay rate of the singular values increases with c_1 : for $c_1 = 0.1$, the singular values decay slowly, indicating that the dynamics are dominated by the small-scale fluctuations; for $c_1 = 5.0$, larger-scale, slow-moving structures dominate the dynamics and the singular values decay faster. The number of POD modes necessary to retain 95% of the energy decreases from $r = 237$ for $c_1 = 0.1$ to $r = 17$ for $c_1 = 5.0$.

Figure 4 plots the first (i.e., the most energetic), 10th, 20th, and 44th POD modes of the density and potential fluctuations for the different c_1 . The POD modes are interpretable: the size of the structures increases with c_1 , which is consistent

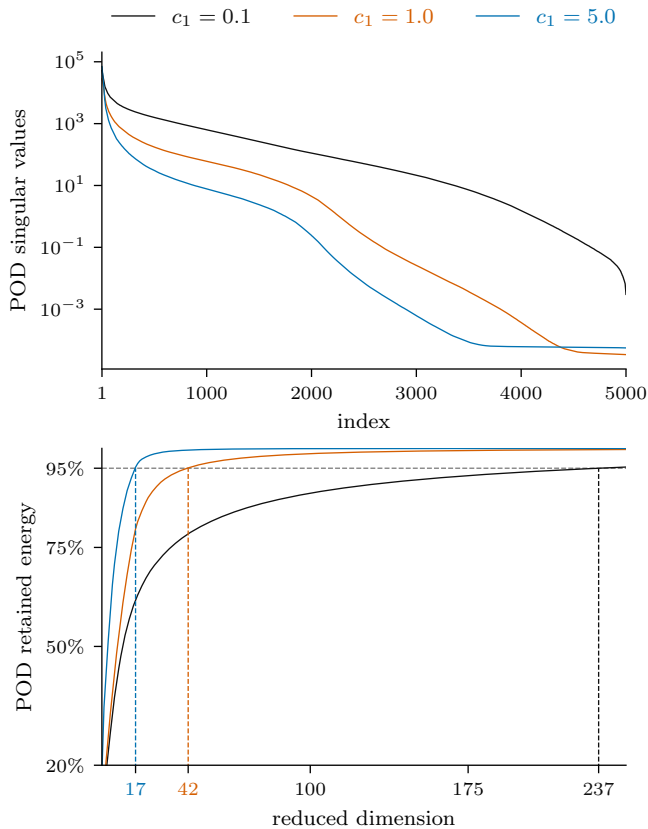


Figure 3. POD singular values (top) and corresponding retained energy (bottom) for $c_1 \in \{0.1, 1.0, 5.0\}$.

with the simulation results in Figure 1 and the decay of the singular values in Figure 3. Moreover, for $c_1 = 0.1$, the POD modes have distinct small-scale features, while for $c_1 = 5.0$ the modes for density and potential are nearly identical.

The choice of the reduced dimension r is essential for a predictive OpInf ROM. Generally, r should be chosen such that (i) the corresponding POD modes retain as much energy as possible and (ii) it is not exceedingly large, to avoid learning an exceedingly large number of ROM coefficients via (8) and (9). For the two cases with more complex dynamics dominated by small scale structures, $c_1 = 0.1$ and $c_1 = 1.0$, we consider OpInf ROMs with reduced dimension $r = 78$. This retains 86.22% and 98.05% of the total energy, respectively. For $c_1 = 5.0$, we consider the reduced dimension $r = 44$, which retains 99.63% of the energy. We note that truncating the POD basis discards higher-order information, meaning that some fine-scale details may not be captured, depending on the truncation level. In problems with turbulent dynamics such as the HW equations, these unresolved structures can be relevant for capturing small-scale turbulent effects. In addition, there is usually a non-negligible interaction between the resolved and unresolved modes. This means that in general, we can only model a subset of the original dynamics, motivating the development of closure models for data-driven ROMs⁵¹.

B. Predictions obtained using Operator Inference

We construct OpInf ROMs following the steps presented in Section III and use them for predictions for 400 additional time units, that is, for a time horizon 400% longer than the training horizon. The learning of the reduced state operators is done via (8). However, since the scale of the projected snapshot data $\hat{\mathbf{Q}} \in \mathbb{R}^{r \times 5,000}$ computed via (6) is different from the scales of the outputs in $\mathbf{Y} \in \mathbb{R}^{2 \times 5,000}$ for all three values of c_1 , we first center (about the temporal mean) and scale (with respect to the maximum absolute value of the centered data) the projected snapshot data prior to inferring the reduced output operator. This ensures that the transformed projected data does not exceed $[-1, 1]$, which is on similar scale as the outputs in \mathbf{Y} . Centering introduces a constant and linear operator in the reduced output (7b) in addition to the original quadratic reduced operator. The learning of the two additional operators is regularized via a hyperparameter $\beta_B \in \mathbb{R}_+$ analogously to the reduced linear operator in Eq. (7a).

To compute the ensemble of solutions, we use a grid of size 10×10 for the regularization parameters in (8) and a grid of size 20×20 for the regularization parameters to infer the transformed reduced output operators for each c_1 . We employ grids with a relatively large cardinality because we want to obtain a comprehensive assessment of the OpInf predictions. In general, grid sizes between 5×5 and 20×20 suffice. We use relative error thresholds of 5% for the means and 30% for the standard deviations of the two outputs of interest, Γ_n and Γ_c . Empirically, we observed that relative error thresholds between 5–10% for the means and between 15–40% for the standard deviations retain models with the desired properties, namely long-time stability and statistical accuracy over the prediction horizon. For a more in-depth analysis, we also extract the solution that minimizes the average relative error of both mean and standard deviation of Γ_n and Γ_c over the prediction time horizon.

Figures 5–7 plot the OpInf approximations for Γ_n and Γ_c , and compare them with the reference high-fidelity results. In orange, we show the ensemble mean and one standard deviation of the OpInf output approximations. In blue, we plot the ensemble solution that minimizes the average relative error of the two outputs over the prediction horizon. We moreover annotate each figure with the estimated means and standard deviations over the prediction horizon.

The OpInf ROMs achieve the primary objective and accurately match the reference means and standard deviations over both the training and prediction horizons. OpInf also approximates some of the overall trends, even though the finer details are not well captured. However, it is important to note that the local features of the reference solutions differ between the training and prediction horizons. Consequently, OpInf ROMs inherently cannot capture some of these features since they were not present in the training dataset. We discuss this point in more detail in Section IV C.

Without regularization, the reduced solutions diverge after only 10–11 time iterations for all c_1 values. In addition, employing commonly used regularization strategies can lead to inaccurate approximations. We illustrate this in Figure 5.

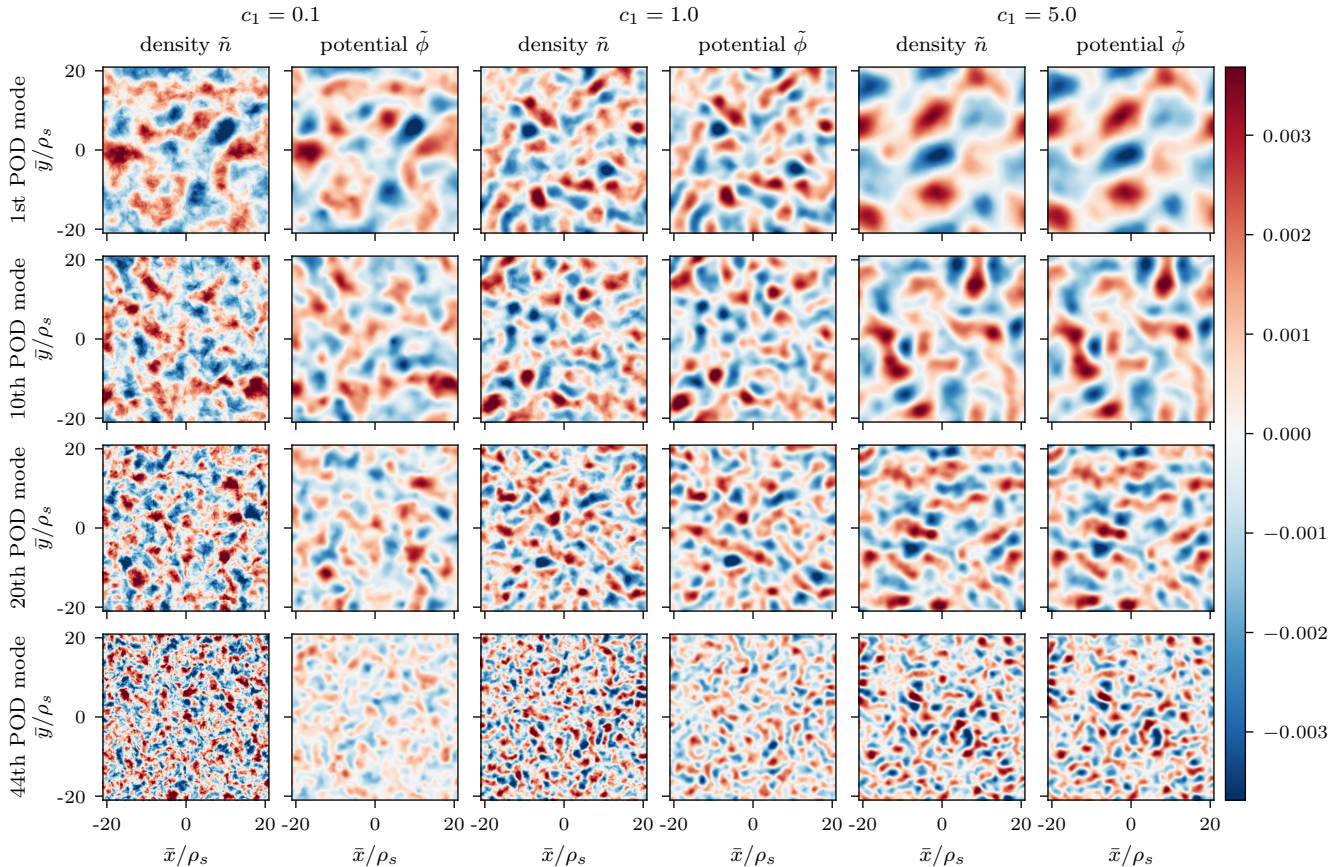


Figure 4. First, 10th, 20th, and 44th POD mode of the density and potential fluctuations for $c_1 \in \{0.1, 1.0, 5.0\}$.

Therein, the green line shows the OpInf approximation obtained via the regularization parameter pair that minimizes the average L_2 relative error for Γ_n and Γ_c over the training horizon excluded diverging solutions. Despite achieving accurate training data approximations, the optimal regularization parameters, determined using the same grid as for the ensemble, resulted in inaccurate predictions.

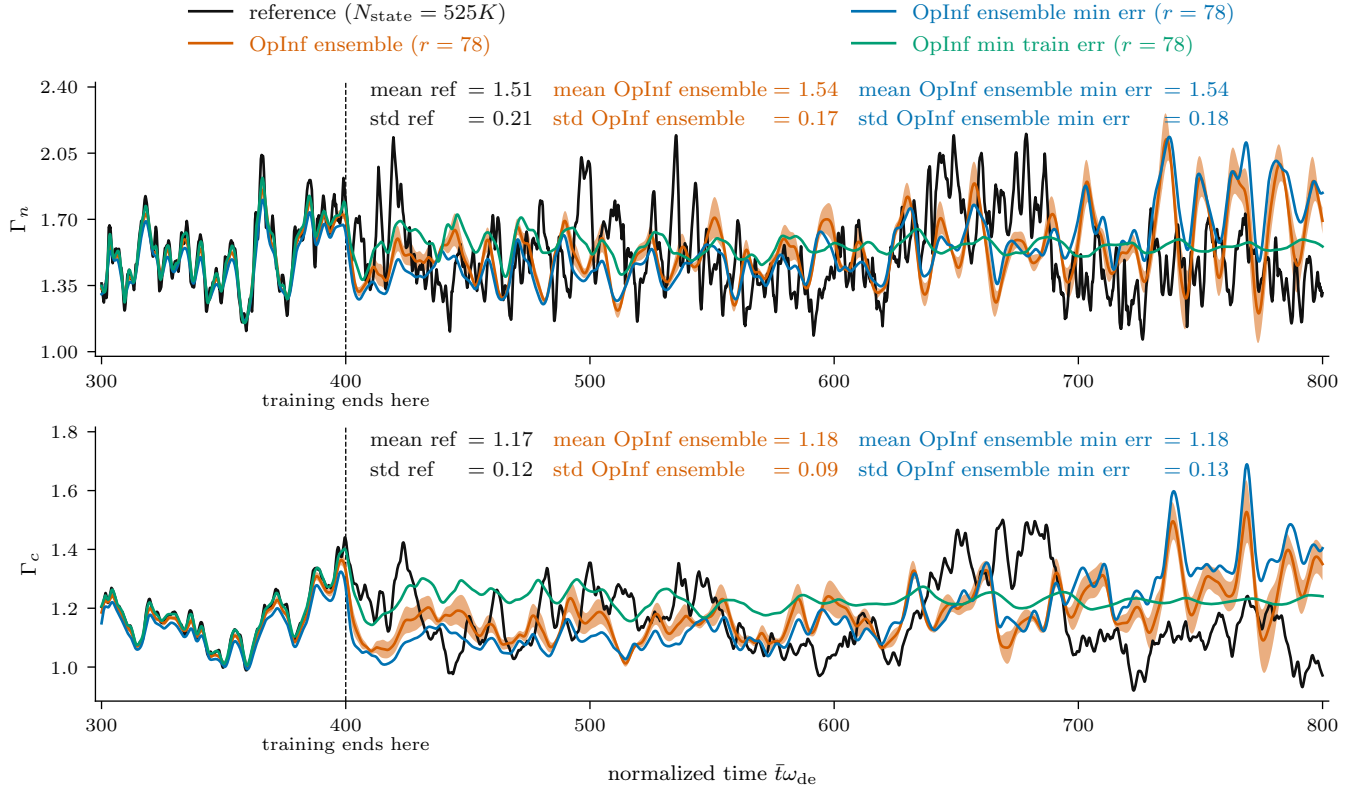
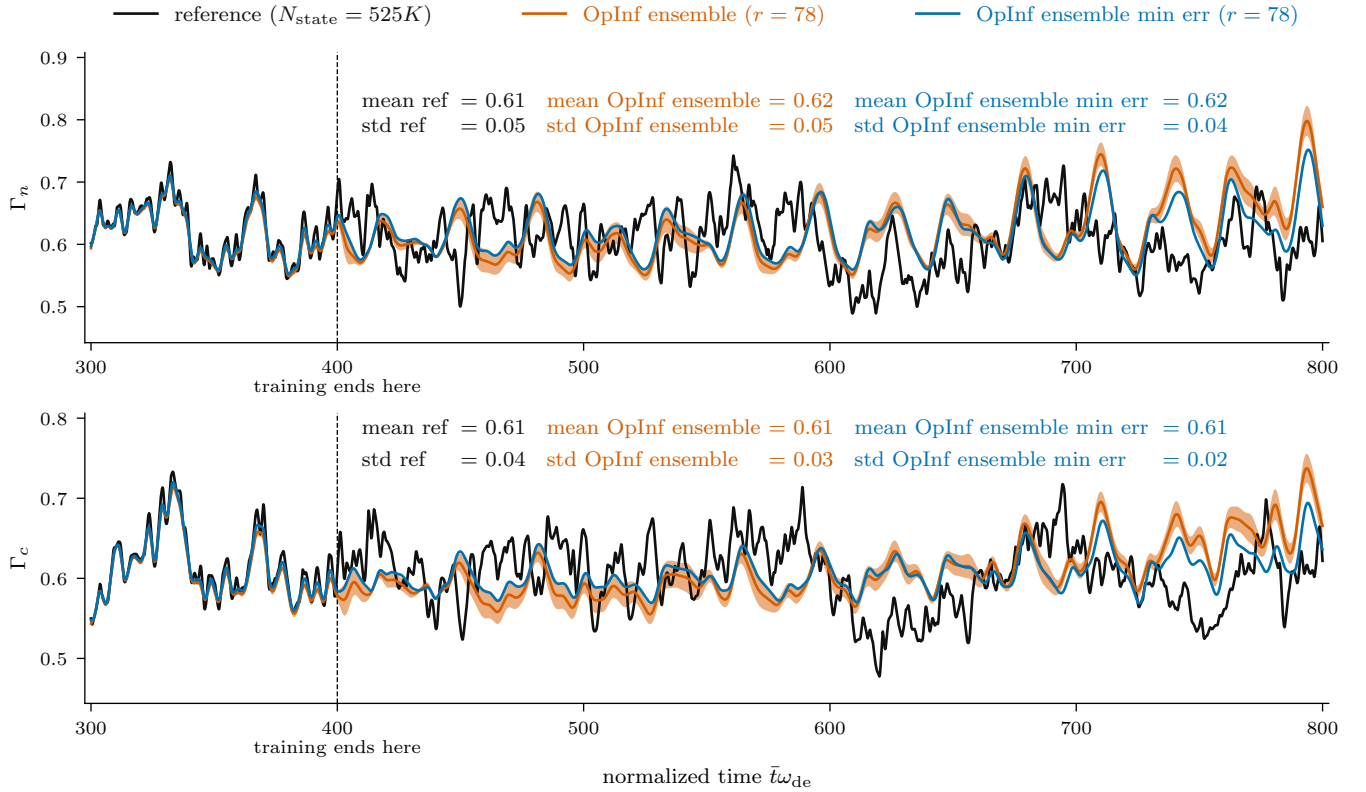
For a more in-depth perspective, we have a closer look at the inferred reduced linear state operators, $\hat{\mathbf{A}} \in \mathbb{R}^{r \times r}$, corresponding to the ensemble solution that minimizes the average prediction error. All three reduced operators have diagonal entries close to 1.0 and off-diagonal elements exhibiting a quasi-band structure with magnitudes smaller than 1.0 that decay as the distance from the diagonal increases. Figure 8 plots the reduced operators off-diagonal entries on the left and their spectra on the right. The eigenvalues of the reduced linear operators lie on or very close to the unit circle in the stability plane. We note that all ensemble solutions exhibited this behavior. Discarded solutions included reduced linear state operators with unstable modes (these solutions typically diverged) as well as strongly damped spectra obtained with large regularization parameters. This positions the spectra at the threshold of linear stability, which allows the linear reduced operators to approximate the oscillatory behavior of the reference solutions. Compared to the spectrum of the linear operator \mathbf{A} of

the HW equations, the originally linearly unstable modes are damped due to regularization. This motivates further exploration into incorporating closure models into our approach and non-linear model reduction techniques^{41,52}.

The runtimes of the OpInf ROMs with reduced dimension $r = 78$, averaged over 100 runs, are 7.024 ± 0.07 seconds for computing the reduced state via (7a) and 0.027 ± 0.0038 seconds for estimating the output using (7b). The corresponding runtimes for the ROM with $r = 44$ are 3.55 ± 0.047 and 0.0048 ± 0.002 seconds, respectively. This translates into four and respectively five orders of magnitude improvement in single-core performance compared the high-fidelity simulations. Solving the ROM and predicting future dynamics is therefore computationally cheap and can be done close to real-time on laptop computers or similar devices.

C. The effect of changing the initial conditions used to generate the training data on the reduced model predictions

We close this section with a discussion regarding the effect of the initial conditions used to generate the high-fidelity training data on the OpInf predictions. While different random initial conditions in the HW system will generate statistically similar outputs over the training and prediction horizons,

Figure 5. OpInf output approximations for $c_1 = 0.1$.Figure 6. OpInf output approximations $c_1 = 1.0$.

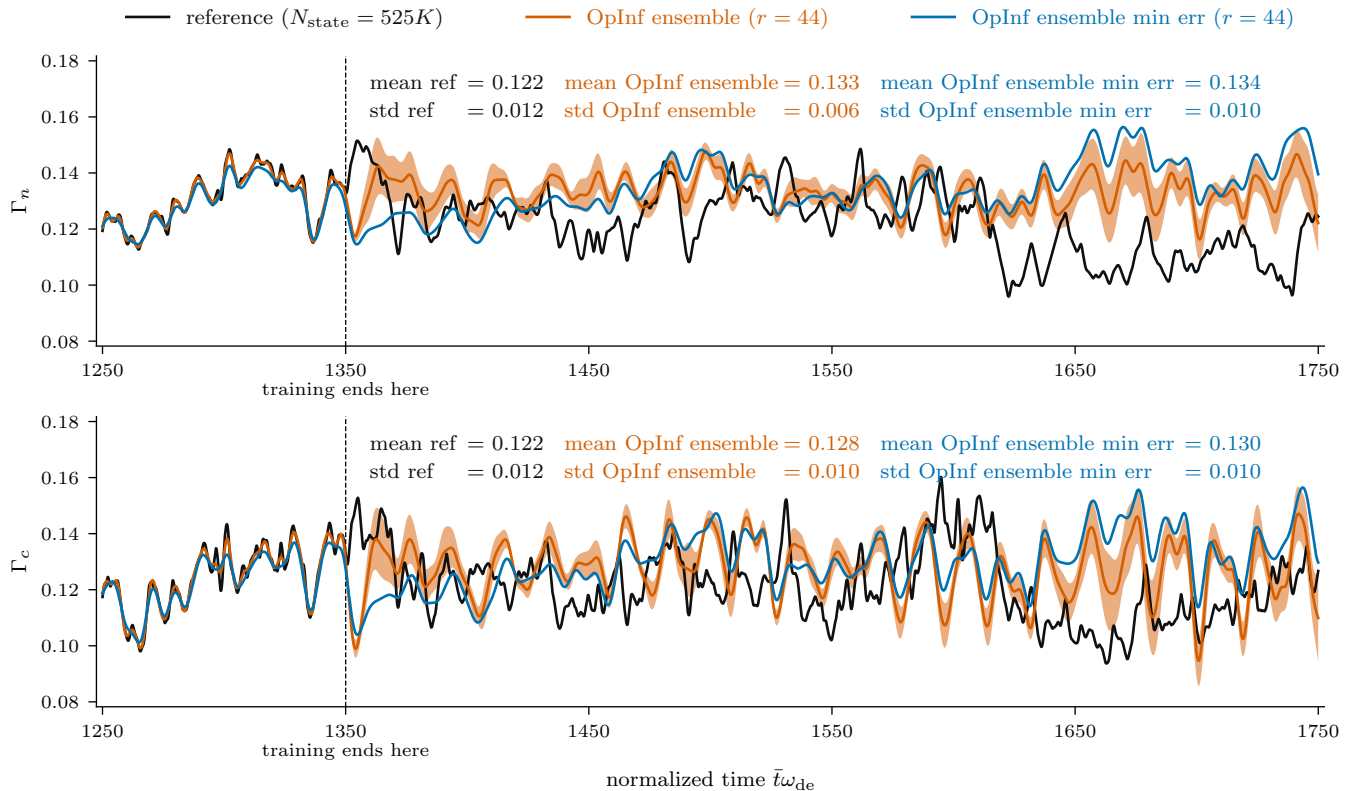


Figure 7. OpInf output approximations for $c_1 = 5.0$.

their local features and trends can diverge due to the system's chaotic nature. Our results in Figures 5, 6 and 7 highlighted this point: the OpInf ROMs accurately captured the statistical properties of the two outputs, but because the reference solutions exhibited differing local features between the training and prediction horizons, the ROM predictions were less effective in capturing this structural change. For a different training dataset for which the trends over training and predictions are more similar, the quality of the ROM predictions can improve. We emphasize this point by performing an additional experiment. The training data were generated in a previous simulation for $c_1 = 1.0$ over the time horizon $[0; 1,000]$ using $\delta t = 0.025$. To ensure that the turbulent dynamics are well developed, we considered $t_{\text{init}} = 500$. We then trained an OpInf ROM using data for 100 time units with reduced dimension $r = 44$, retaining 95% of the total energy. Similar to the experiments discussed above, we used the ROM for predictions for 400 additional time units. Using a relative error threshold of 5% for the means and 15% for the standard deviations, Figure 9 shows that the OpInf ROM predictions accurately match the reference statistics and capture the trends of the reference solutions over the prediction horizon. The similarity between the trends of the reference solution over the training and prediction horizons was crucial for obtaining these results. Two strategies can be employed to mitigate the influence of a specific initial condition on the long-term behavior of the ROM and enhance its robustness: extending the training horizon or utilizing a training dataset that incorporates trajectories from

multiple initial conditions. However, it is important to acknowledge that both approaches come with an increased computational cost for generating the training data.

V. SUMMARY AND CONCLUSIONS

In this paper, we showed that Scientific Machine Learning can be used to construct predictive reduced models from data for complex plasma turbulence models such as the Hasegawa-Wakatani equations. To this end, we proposed using Operator Inference. This approach is flexible and easy to use, and only requires knowledge about the structure of the underlying governing equations and data to train a structure-preserving reduced model. Our results showed that Operator Inference can be employed to construct reduced models that capture the important features of the turbulent dynamics and generalize beyond the training horizon while reducing the computational effort by up to five orders of magnitude. This in turn enables performing these simulations on laptop computers or similar devices instead of using compute clusters or supercomputers. In the broader context of fusion research, constructing such reduced models can have a significant impact and amount to a milestone towards real-time plasma turbulence simulations as well as the design of optimized fusion devices. While these results illustrate the potential of the approach, they also highlight a number of open questions. Important future directions include the investigation of closure models to account

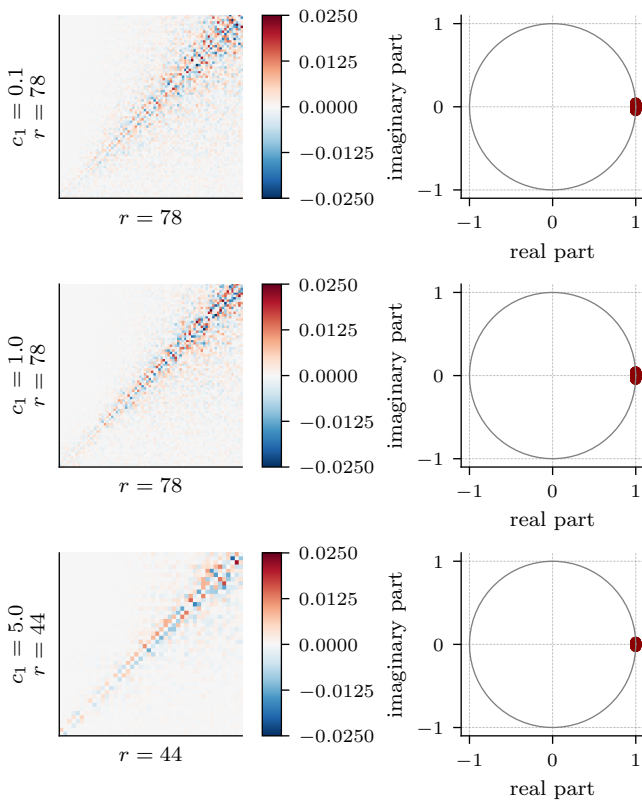


Figure 8. Left: off-diagonal entries of the reduced linear state operators. Right: the corresponding spectra.

for the truncated proper orthogonal decomposition modes and the interaction between the resolved and unresolved modes. An alternative direction involves investigating non-linear approaches for model reduction such as Neural Operators⁴¹ and Neural Galerkin schemes⁵² that were shown to be effective in approximating complex dynamics.

ACKNOWLEDGMENTS

The authors gratefully acknowledge Robin Greif and Andreas Stegmeir for fruitful discussions. C.Gahr was supported by the Helmholtz Association under the joint research school “Munich School for Data Science – MUDS”. Computations were performed on the HPC system Cobra at the Max Planck Computing and Data Facility.

DATA AVAILABILITY STATEMENT

The high-fidelity simulation data were generated using the `hw2d` code⁴⁴. The code and data to reproduce the results of this paper are available at <https://gitlab.mpcdf.mpg.de/cgahr/learning-roms-for-hw>.

REFERENCES

- ¹S. Atchley, C. Zimmer, J. Lange, D. Bernholdt, V. Melesse Vergara, T. Beck, M. Brim, R. Budiardja, S. Chandrasekaran, M. Eisenbach, T. Evans, M. Ezell, N. Frontiere, A. Georgiadou, J. Glenski, P. Grete, S. Hamilton, J. Holmen, A. Huebl, D. Jacobson, W. Joubert, K. McMahon, E. Merzari, S. Moore, A. Myers, S. Nichols, S. Oral, T. Papatheodore, D. Perez, D. M. Rogers, E. Schneider, J.-L. Vay, and P. K. Yeung, in *Proceedings of the International Conference for High Performance Computing, Networking, Storage and Analysis, SC '23* (Association for Computing Machinery, New York, NY, USA, 2023) pp. 1–16.
- ²E. A. Belli, J. Candy, and I. Sfiligoi, *Plasma Physics and Controlled Fusion* **65**, 024001 (2022).
- ³I.-G. Farcas, G. Merlo, and F. Jenko, *Communications Engineering* **1**, 43 (2022).
- ⁴P. Benner, M. Ohlberger, A. Cohen, and K. Willcox, *Model Reduction and Approximation*, Computational Science & Engineering (Society for Industrial and Applied Mathematics, 2017).
- ⁵P. Benner, S. Gugercin, and K. Willcox, *SIAM Review* **57**, 483 (2015).
- ⁶B. Peherstorfer and K. Willcox, *Computer Methods in Applied Mechanics and Engineering* **306**, 196 (2016).
- ⁷B. Kramer, B. Peherstorfer, and K. E. Willcox, *Annual Review of Fluid Mechanics* **56**, 521 (2024).
- ⁸B. Kramer and K. E. Willcox, *AIAA Journal* **57**, 2297 (2019).
- ⁹E. Qian, B. Kramer, B. Peherstorfer, and K. Willcox, *Physica D: Nonlinear Phenomena* **406**, 132401 (2020).
- ¹⁰I. Farcas, R. Gundevia, R. Munipalli, and K. E. Willcox, in *AIAA SCITECH 2023 Forum* (American Institute of Aeronautics and Astronautics, 2023).
- ¹¹E. Qian, I.-G. Farcas, and K. Willcox, *SIAM Journal on Scientific Computing* **44**, A1934 (2022).
- ¹²R. Swischuk, B. Kramer, C. Huang, and K. Willcox, *AIAA Journal* **58**, 2658 (2020).
- ¹³O. Issan and B. Kramer, *Journal of Computational Physics* **473**, 111689 (2023).
- ¹⁴P. Khodabakhshi and K. E. Willcox, *Computer Methods in Applied Mechanics and Engineering* **389**, 114296 (2022).
- ¹⁵J. L. d. S. Almeida, A. C. Pires, K. F. V. Cid, and A. C. N. Junior, “Non-Intrusive Reduced Models based on Operator Inference for Chaotic Systems,” (2022), arxiv:2206.01604 [nlin].
- ¹⁶I. Farcas, R. Munipalli, and K. E. Willcox, in *AIAA AVIATION 2022 Forum*, AIAA AVIATION Forum (American Institute of Aeronautics and Astronautics, 2022).
- ¹⁷W. I. T. Uy, D. Hartmann, and B. Peherstorfer, *Computers & Mathematics with Applications* **145**, 224 (2023).
- ¹⁸R. Geelen and K. Willcox, *Philosophical Transactions of the Royal Society A: Mathematical, Physical and Engineering Sciences* **380**, 20210206 (2022).
- ¹⁹I.-G. Farcas, R. P. Gundevia, R. Munipalli, and K. E. Willcox, “Improving the accuracy and scalability of large-scale physics-based data-driven reduced modeling via domain decomposition,” (2023), accepted for publication in *AIAA Journal*, arxiv:2311.00883 [cs, math].
- ²⁰R. Geelen, S. Wright, and K. Willcox, *Computer Methods in Applied Mechanics and Engineering* **403**, 115717 (2023).
- ²¹A. Hasegawa and M. Wakatani, *Physical Review Letters* **50**, 682 (1983).
- ²²S. J. Camargo, D. Biskamp, and B. D. Scott, *Physics of Plasmas* **2**, 48 (1995).
- ²³P. Manz, *The Microscopic Picture of Plasma Edge Turbulence*, habilitation, Technische Universität München (2019).
- ²⁴R. Numata, R. Ball, and R. L. Dewar, *Physics of Plasmas* **14**, 102312 (2007).
- ²⁵M. Sasaki, T. Kobayashi, R. O. Dendy, Y. Kawachi, H. Arakawa, and S. Inagaki, *Plasma Physics and Controlled Fusion* **63**, 025004 (2020).
- ²⁶G. Yatomi, M. Nakata, and M. Sasaki, *Plasma Physics and Controlled Fusion* **65**, 095014 (2023).
- ²⁷G. Berkooz, P. Holmes, and J. L. Lumley, *Annual Review of Fluid Mechanics* **25**, 539 (1993).
- ²⁸I. R. Goumiri, C. W. Rowley, Z. Ma, D. A. Gates, J. A. Krommes, and J. B. Parker, *Physics of Plasmas* **20**, 042501 (2013).
- ²⁹J. Castagna, F. Schiavello, L. Zanisi, and J. Williams, *Physics of Plasmas* **31**, 033902 (2024).

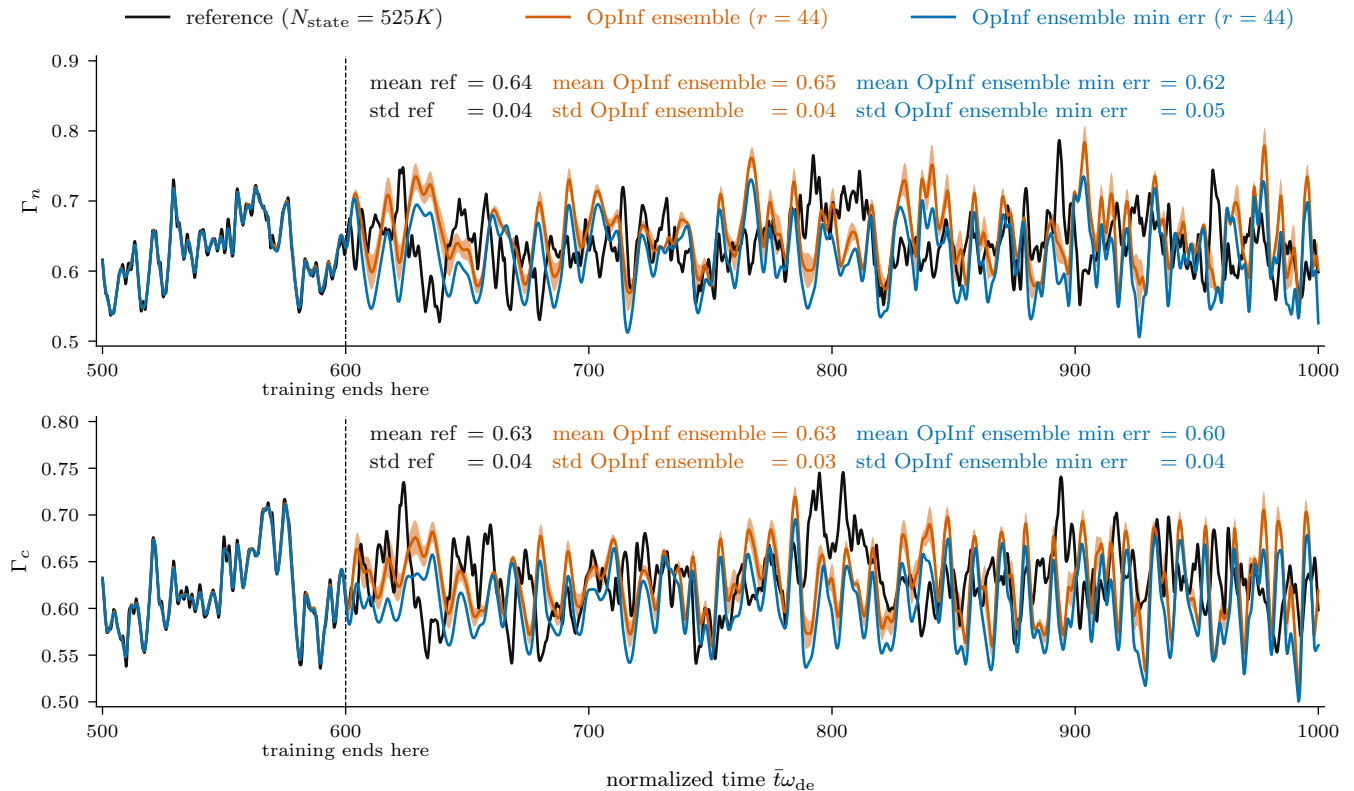


Figure 9. OpInf output approximations $c_1 = 1.0$ for a different initial condition.

- ³⁰R. Greif, F. Jenko, and N. Thurey, “Physics-Preserving AI-Accelerated Simulations of Plasma Turbulence,” (2023), arxiv:2309.16400 [physics].
- ³¹B. Clavier, D. Zarzoso, D. del-Castillo-Negrete, and E. Frenord, “A generative machine learning surrogate model of plasma turbulence,” (2024), arxiv:2405.13232 [physics].
- ³²R. A. Heinson and P. H. Diamond, *Physical Review E* **101**, 061201 (2020).
- ³³Z. Lin, T. Maurel-Oujia, B. Kadoch, P. Krah, N. Saura, S. Benkadda, and K. Schneider, *Physics of Plasmas* **31**, 032505 (2024).
- ³⁴F. Faraji, M. Reza, A. Knoll, and J. N. Kutz, *Journal of Physics D: Applied Physics* **57**, 065201 (2023).
- ³⁵S. Futatani, S. Benkadda, and D. del-Castillo-Negrete, *Physics of Plasmas* **16**, 042506 (2009).
- ³⁶A. Kusaba, T. Kuboyama, and S. Inagaki, *Plasma and Fusion Research* **15**, 1301001 (2020).
- ³⁷R. Taylor, J. N. Kutz, K. Morgan, and B. Nelson, *Review of Scientific Instruments* **89**, 053501 (2018), arxiv:1702.06871.
- ³⁸F. Faraji, M. Reza, A. Knoll, and J. N. Kutz, *Journal of Physics D: Applied Physics* **57**, 065202 (2023).
- ³⁹A. A. Kaptanoglu, K. D. Morgan, C. J. Hansen, and S. L. Brunton, *Physics of Plasmas* **27**, 032108 (2020).
- ⁴⁰Y. Jajima, M. Sasaki, R. T. Ishikawa, M. Nakata, T. Kobayashi, Y. Kawachi, and H. Arakawa, *Plasma Physics and Controlled Fusion* **65**, 125003 (2023).
- ⁴¹V. Gopakumar, S. Pamela, L. Zanisi, Z. Li, A. Gray, D. Brennan, N. Bhatia, G. Stathopoulos, M. Kusner, M. P. Deisenroth, A. Anandkumar, the JOREK Team, and M. Team, *Nuclear Fusion* **64**, 056025 (2024).
- ⁴²M. Wakatani and A. Hasegawa, *The Physics of Fluids* **27**, 611 (1984).
- ⁴³A. Hasegawa and K. Mima, *Physics of Fluids* **21**, 87 (1978).
- ⁴⁴R. Greif, *Journal of Open Source Software* **8**, 5959 (2023).
- ⁴⁵A. Arakawa, *Journal of computational physics* **135**, 103 (1997).
- ⁴⁶C. Runge, *Mathematische Annalen* **46**, 167 (1895).
- ⁴⁷G. H. Golub and C. F. V. Loan, *Matrix Computations* (The Johns Hopkins University Press, 2013).
- ⁴⁸S. A. McQuarrie, C. Huang, and K. E. Willcox, *Journal of the Royal Society of New Zealand* **51**, 194 (2021).
- ⁴⁹C. R. Harris, K. J. Millman, S. J. van der Walt, R. Gommers, P. Virtanen, D. Cournapeau, E. Wieser, J. Taylor, S. Berg, N. J. Smith, R. Kern, M. Picus, S. Hoyer, M. H. van Kerkwijk, M. Brett, A. Haldane, J. F. del Río, M. Wiebe, P. Peterson, P. Gérard-Marchant, K. Sheppard, T. Reddy, W. Weckesser, H. Abbasi, C. Gohlke, and T. E. Oliphant, *Nature* **585**, 357 (2020).
- ⁵⁰P. Virtanen, R. Gommers, T. E. Oliphant, M. Haberland, T. Reddy, D. Cournapeau, E. Burovski, P. Peterson, W. Weckesser, J. Bright, S. J. van der Walt, M. Brett, J. Wilson, K. J. Millman, N. Mayorov, A. R. J. Nelson, E. Jones, R. Kern, E. Larson, C. J. Carey, Í. Polat, Y. Feng, E. W. Moore, J. VanderPlas, D. Laxalde, J. Perktold, R. Cimrman, I. Henriksen, E. A. Quintero, C. R. Harris, A. M. Archibald, A. H. Ribeiro, F. Pedregosa, P. van Mulbregt, and SciPy 1.0 Contributors, *Nature Methods* **17**, 261 (2020).
- ⁵¹S. E. Ahmed, S. Pawar, O. San, A. Rasheed, T. Iliescu, and B. R. Noack, *Physics of Fluids* **33**, 091301 (2021).
- ⁵²J. Bruna, B. Peherstorfer, and E. Vanden-Eijnden, *Journal of Computational Physics* **496**, 112588 (2024).